Covalent Triazine Frameworks and Porous Carbons: Perspective from an Azulene-Based Case

Jiang, K.; Peng, P.; Tranca, D.; Tong, G.; Ke, C.; Lu, C.; Hu, J.; Liang, H.; Li, J.; Zhou, S.; Kymakis, E.; Zhuang, X.;

Originally published:

June 2022

Macromolecular Rapid Communications 43(2022), 2200392

DOI: https://doi.org/10.1002/marc.202200392

Covalent Triazine Frameworks and Porous Carbons: Perspective from an Azulene-Based Case

Kaiyue Jiang, Peipei Peng, Diana Tranca, Gangsheng Tong, Changchun Ke, Chenbao Lu, Jun Hu, Haiwei Liang, Jiantong Li, Shengqiang Zhou, Emmanuel Kymakis, Xiaodong Zhuang

Abstract

Covalent triazine frameworks (CTFs) are among the most valuable frameworks owing to many fantastic properties. However, molten salt-involved preparation of CTFs at 400–600 °C causes debate on whether CTFs represent organic frameworks or carbon. Herein, new CTFs based on the 1,3-dicyanoazulene monomer (CTF-Azs) are synthesized using molten $ZnCl_2$ at 400–600 °C. Chemical structure analysis reveals that the CTF-Az prepared at low temperature (400 °C) exhibits polymeric features, whereas those prepared at high temperatures (600 °C) exhibit typical carbon features. Even after being treated at even higher temperatures, the CTF-Azs retain their rich porosity, but the polymeric features vanish. Although structural de-conformation is a widely accepted outcome in polymer-to-carbon rearrangement processes, the study evaluates such processes in the context of CTF systems. A proof-of-concept study is performed, observing that the as-synthesized CTF-Azs exhibit promising performance as cathodes for Li- and K-ion batteries. Moreover, the as-prepared NPCs exhibit excellent catalytic oxygen reduction reaction (ORR) performance; hence, they can be used as air cathodes in Zn-air batteries. This study not only provides new building blocks for novel CTFs with controllable polymer/carbon features but also offers insights into the formation and structure transformation history of CTFs during thermal treatment.

1 Introduction

Covalent triazine frameworks (CTFs) have attracted considerable interest and have emerged as a new class of porous organic materials since the pioneering work of Thomas and coworkers on microporous polytriazine networks.[1] Owing to their defined triazine-based structure and ultrahigh porosity, CTFs have shown great potential in diverse fields, including gas adsorption,[2] sensor,[3] catalyst,[4] and catalyst support[5] applications. In addition to the earliest ionothermal approach that entails the use of zinc chloride ($ZnCl_2$), other CTF preparation strategies have been developed over the past decades to address the confusion pertaining to the porous carbon (PC) properties of CTFs prepared under high temperatures. Typically, numerous CTFs with diverse types of novel building blocks have been prepared using a strong Brønsted acid in the presence of a superacid[6] or using the Friedel–Crafts reaction in the presence of aluminum chloride ($AlCl_3$).[7] However, determining whether most of these CTFs are ordered or amorphous is difficult. Moreover, studies have yet to characterize their crystallization behavior through methods such as X-ray diffraction (XRD) analysis (for peak assignment); hence, the boundary between polymers and carbon in the case of the newly developed CTFs has become increasingly blurred.[7]

Both CTFs and their carbon derivatives have diverse applications in the energy field. In general, CTFs with typical semiconductor characteristics have potential for use in photocatalysis[8] and photoelectrocatalysis[9] and as organic electrode materials.[10] CTF-derived PCs are suitable for use in electrocatalysis owing to their high conductivity and ultrahigh-specific surface area (SSA). Additionally, CTFs exhibit high stability because their aromatic triazine core is extremely stable and rich in nitrogen.[11] However, the polymeric and carbon characteristics of CTFs prepared under high temperatures are unclear, and this ambiguity has led to unsystematic design strategies. Therefore, scholars must provide a systematic CTF preparation process and

investigate the boundary between the polymeric and carbon features of CTFs and the corresponding PCs.

Accordingly, the present study developed a rational strategy for preparing azulene-based CTFs (hereafter referred to as CTF-Azs) and the corresponding PCs by using ionothermal synthesis or extra pyrolysis and activation treatments. The azulene-to-naphthalene rearrangement process was applied to understand the intrinsic ultrahigh porosity of both the as-prepared CTFs and PCs with rich topological defects. These new porous materials were determined to exhibit potential for use in energy applications. For example, the as-prepared CTFs exhibited performance in a K^+ energy storage device with a specific capacity of 120 mA h g^{-1} at 1 A g^{-1} after 100 cycles. Moreover, the study prepared N-doped PCs (NPCs) and observed that they exhibited an extremely positive onset potential (0.866 V), which was comparable to that of Pt/C (0.895 V). When used as air cathodes, the as-prepared NPCs achieved excellent Zn–air battery performance with a power density of 141.8 mW cm^{-2}, which was considerably higher than that of Pt/C (101.1 mW cm^{-2}). These results indicate that the proposed azulene-based strategy can be used to prepare porous materials that are rich in both N and topological defects and are versatile for use in energy-related applications.

2 Results and Discussion

This study synthesized CTF-Azs by using molten $ZnCl_2$-assisted ionothermal synthesis (details in Supporting Information) based on a newly designed benzene-free monomer, namely 1,3-dicyanoazulene, which is a typical naphthalene isomer (**Figure** 1 and Figure S1, Supporting Information).[1, 12] Specifically, the CTF-Azs were prepared at 400, 400/600, and 600 °C and are denoted herein as CTF-Az-400, CTF-Az-400/600, and CTF-Az-600, respectively. Subsequently, the CTF-Azs were used as precursors to prepare PCs through pyrolysis and ammonia activation at 800, 900, and 1000 °C.; the PCs prepared without ammonia activation at 800, 900, and 1000 °C are denoted herein as PC-800, PC-900, and PC-1000, respectively, and those prepared with ammonia activation at these temperatures are denoted herein as PC-800a, PC-900a, and PC-1000a, respectively. We also prepared control samples (CTF-Naph, CTF-Naph-400, and CTF-Naph-600; PC-Naph-900a) by using identical approaches (Scheme S2, Supporting Information) based on a naphthalene monomer. Furthermore, to explain the partial carbonization caused by the high reaction temperatures, we developed three theoretical models (models A–C; Figure 1b), with model A representing a structure involving an ideal connection of triazine with three staggered azulene arms (indicated in red, yellow, and purple in Figure S5, Supporting Information). According to this structure, the thermal dehydrogenation process resulted in the production of new C-C bonds, and five-seven-membered rings were converted to hexagonal rings, possibly representing the transition from the CTF-Az to PCs. Accordingly, our strategy can produce a new benzene-free monomer that can serve as the basis for preparing novel CTFs that exhibit carbon properties.

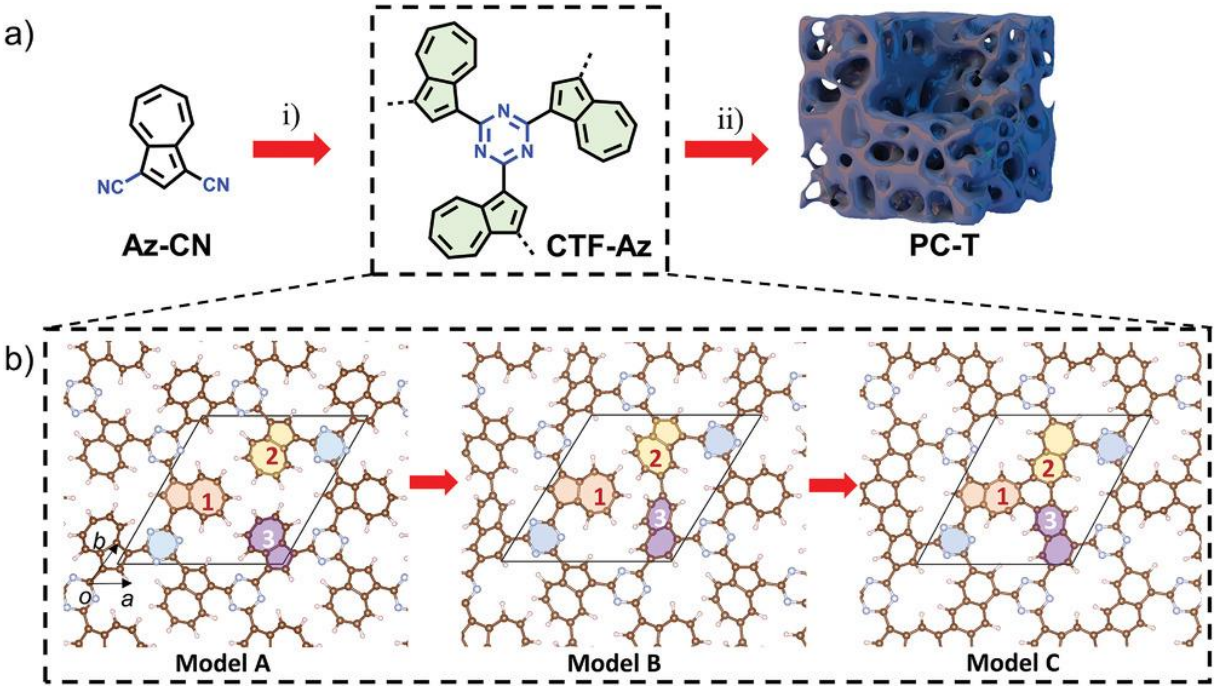

Figure 1a) Synthetic approach for the CTF-Azs and PCs with coexisting topological/heteroatom defects. i) $ZnCl_2$, 400–600 °C; ii) N_2, 800–1000 °C, 2 h; or with subsequent ammonia treatment for 20 min at 800 °C. b) Proposed theoretical models of samples in different states during the transition from CTFs to partially PC-based CTFs.

We performed Fourier-transform infrared (FT-IR) spectroscopy to study the chemical structures of the CTF-Azs (**Figure** 2a). The FT-IR spectra revealed bands at 1617 cm^{-1} (aromatic C-N stretching mode)[13] and 1385 cm^{-1} (in-plane ring stretching vibration),[14] which indicated the successful formation of triazine rings; this was determined to be consistent with a previous report indicating the disappearance of the carbonitrile band at 2220 cm^{-1}.[1] X-ray diffraction (XRD) was also performed for the CTF-Azs. The XRD patterns (Figure 2f) revealed a broad peak at 4.0° for CTF-Az-400; nevertheless, such a peak was not observed for the other two samples, and this can be attributed to their higher degree of carbonization at higher temperatures. Moreover, we executed X-ray absorption near-edge structure (XANES) spectroscopy to determine the chemical environments of C and N in the CTFs (Figure 2b,c). The C K-edge XANES spectrum displayed two obvious peaks at 286.5 and 293.2 eV, which were ascribed to the π^* resonance of sp^2-hybridized N-C=N atoms in the triazine rings[15] and C-C σ^* states, respectively.[16] The spectrum indicated another shoulder-shaped peak at 288.3–289.0 eV, which was attributed to the σ^* resonance of C-N-C[17] or carbon atoms attached to oxygen.[18] In addition, the N K-edge XANES spectrum revealed three absorption peaks, which were ascribed to sp^2-hybridized pyridinic-N and pyrrolic-N (≈399.7 1 eV), graphitic-N (402.7 eV), and C-N σ^* transitions in the aromatic C-N-C portion of triazine (≈408.6 eV).[19] X-ray photoelectron spectroscopy (XPS) was also used to further identify the structural characteristics of CTF-Az-400/600. The XPS spectrum (Figure S6a, Supporting Information) revealed the presence of C, O, and N. The spectrum also indicated C 1s deconvoluted peaks at 285.0, 286.3, and 287.6 eV, which were attributed to C-C/C=C, C=N, and C-N/C-O bonds, respectively (Figure 2b).[20] Four different N configurations were observed in the N 1s spectrum (Figure 2c), namely pyridinic-N (398.6 eV), pyrrolic-N (400.1 eV), graphitic-N (401.3 eV), and oxidized-N (403.4 eV) configurations, which were determined to be consistent with the XANES results.[19, 21] We also performed XPS analyses for the other CTF samples; the spectrum for CTF-Az-600 indicated the presence of graphitic-N (Figure S6c, Supporting Information), but that for CTF-Az-400 did not indicate the presence of graphitic-N, indicating that graphitic-N exists only above a specific temperature. These results indicate that the CTF-Azs synthesized

at temperatures exceeding 400 °C were partially carbonized and different from those prepared under typical 400 °C conditions.

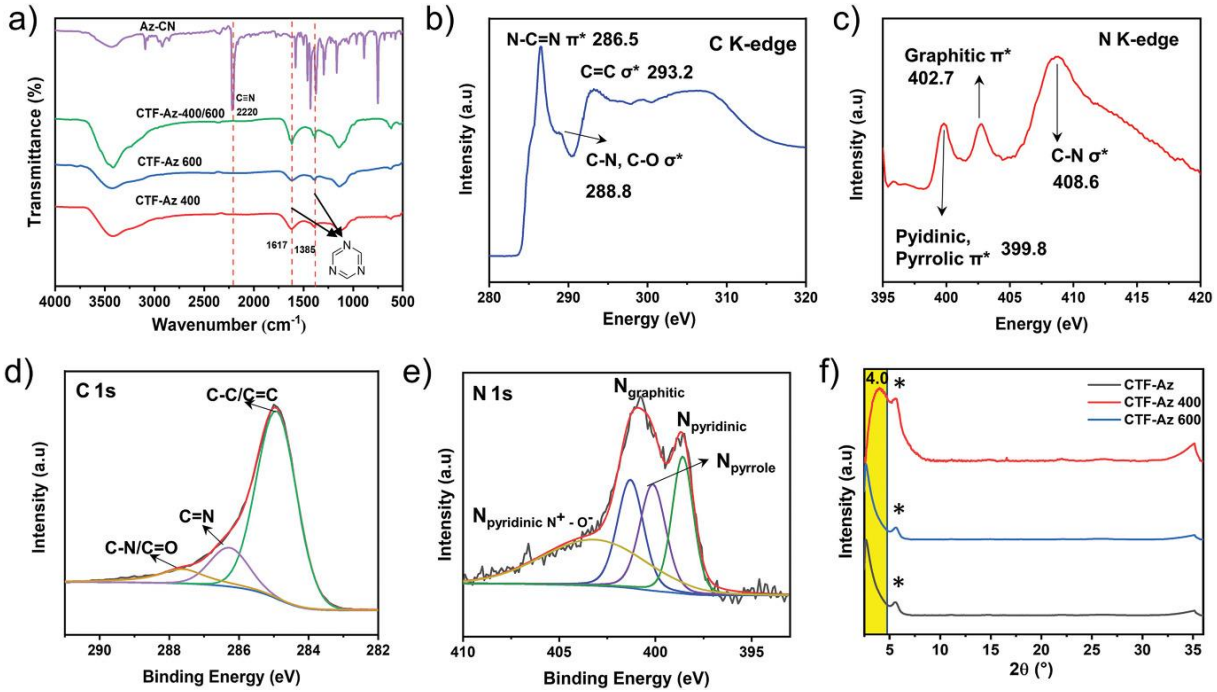

Figure 2 Chemical structure analysis results for CTF-Azs. a) FT-IR spectra of Az-CN (purple), CTF-Az-400/600 (green), CTF-Az-400 (red), and CTF-Az-600 (blue). b) C K-edge and c) N K-edge XANES spectra of the CTF-Az-400/600. d) C 1s XPS spectra and e) N 1s spectra of the CTF-Az-400/600. f) XRD spectra of CTF-Az-400/600, CTF-Az-400, and CTF-Az-600. (Peak at 4.0 represents local crystallization in the CTF-Az-400 sample; peaks located at * position are from the Kapton tape.)

Raman spectra (Figure S7, Supporting Information) for the CTF-Azs displayed obvious D (≈1345 cm^{-1}) and G (≈1593 cm^{-1}) bands. The I_D/I_G ratio derived for CTF-Az-400 was 1.03, which was considerably higher than those derived for CTF-Az-600 (0.91) and CTF-Az-400/600 (0.91); this result indicates that CTF-Az-400 had a higher quantity of azulene and lower degree of carbonization than did the other samples (Table S1, Supporting Information).[22] Furthermore, thermogravimetric analysis (Figure S8, Supporting Information) revealed that the CTF-Azs had excellent thermal stability and could be readily transformed to carbon at yield rates ranging from 85% to 94% at 800 °C. We also conducted nitrogen physisorption measurements to obtain insight into the porous nature of the CTF-Azs, and we derived type IV isotherms as a result (Figure S9a, Supporting Information).[23] We constructed pore size distribution curves (Figure S9b, Supporting Information) for the samples by using density functional theory (DFT); the curves indicated that the samples exhibited both microporous and mesoporous structures. Furthermore, we measured the SSAs of the samples (**Table** 1), and the results indicated that among the as-prepared CTF-Azs, CTF-Az-400 exhibited the highest SSA (1755 m^2 g^{-1}). Scanning electron microscopy and transmission electron microscopy (TEM) were used to visualize the morphology of the CTF-Azs. The results revealed that the CTF-Azs were composed of small, irregular particles that were stacked together (Figure S10, Supporting Information). Specifically, the TEM images (Figure S11a, Supporting Information) depicted a graphitic layered structure at the edges.[24] In addition, we executed energy-dispersive spectroscopy (EDS) for elemental mapping; the results demonstrated homogeneously distributed C and N atoms in the CTF-Azs.[25]

Table 1. N_2 physisorption property of as-prepared samples

Sample names	S_{BET} [m^2 g^{-1}]	S_{Lang} [m^2 g^{-1}]	S_{micro} [m^2 g^{-1}]	V_{micro} [m^2 g^{-1}]	V_{total} [cm^3 g^{-1}]	D_{av} [cm^3 nm]
CTF-Az-400/600	1716	2622	590	0.27	3.29	7.7
CTF-Az-600	1639	2486	661	0.31	3.22	7.9
CTF-Az-400	1755	2617	727	0.33	3.18	7.3
PC-800	1551	2359	549	0.26	3.12	8.1
PC-900	1478	2244	517	0.24	2.93	7.9
PC-1000	1526	2295	584	0.27	2.98	7.8
PC-800a	1607	2457	561	0.26	3.22	8.0
PC-900a	1847	2854	474	0.22	3.66	7.9
PC-1000a	1701	2593	580	0.27	3.33	7.8

We performed electron spin resonance (ESR) spectroscopy on the samples. The spectra indicated that the ESR signal intensity detected for CTF-Az-400/600 was greater than that detected for CTF-Naph (Figure S12, Supporting Information), demonstrating that the ESR signal of CTF-Az-400/600 was mainly derived from the embedded azulene.[26] The ESR spectra (**Figure** 3a) also revealed unpaired spins in the CTF-Azs samples, which were due to the embedded azulene; the number of these spins decreased as the reaction temperature increased. Furthermore, zero-field-cooled and field-cooled magnetization curves were plotted for CTF-Az-400 (Figure 3b), and the curves showed a typical separation feature at approximately room temperature. Notably, the remnant magnetization observed at 300 K was not reduced to zero, suggesting the existence of magnetic ordering even at 300 K (Figure S13, Supporting Information). This high-temperature ordering in CTF-Az-400 can be attributed to the rich free radicals originating from the rich azulene units.[27] In addition, we analyzed the variation of magnetization as a function of the applied magnetic field at 300 K. We noted a relatively small magnetic hysteresis loop in CTF-Az-400, further confirming the magnetic ordering in this sample at room temperature (Figure 3c).[28] As mentioned, we constructed three models, namely models A–C, and evaluated their corresponding band structures and densities of states (DOS) to describe the states existing during the formation of the CTF-Azs (Figure 3d). We noted that the band gaps decreased slightly from 1.71 to 1.52 eV as the fraction of conjugation-fused structures and the proportion of hexagonal (benzene) rings increased; the DOS values also exhibited a similar decrease because the conductive band minimum shifted downward (Figure 3e). To determine the contributions of specific components of the various models, we executed a projected DOS analysis (Figures S14–S16, Supporting Information). It could be seen clearly that azulene unit connected via dehydrogenation contributes more to valence bands. These results indicate that in the proposed strategy, the optoelectronic and magnetic features of the as-prepared CTF-Azs could be systematically controlled by controlling the azulene unit content (or the azulene-to-naphthalene process) through treatment at different temperatures.

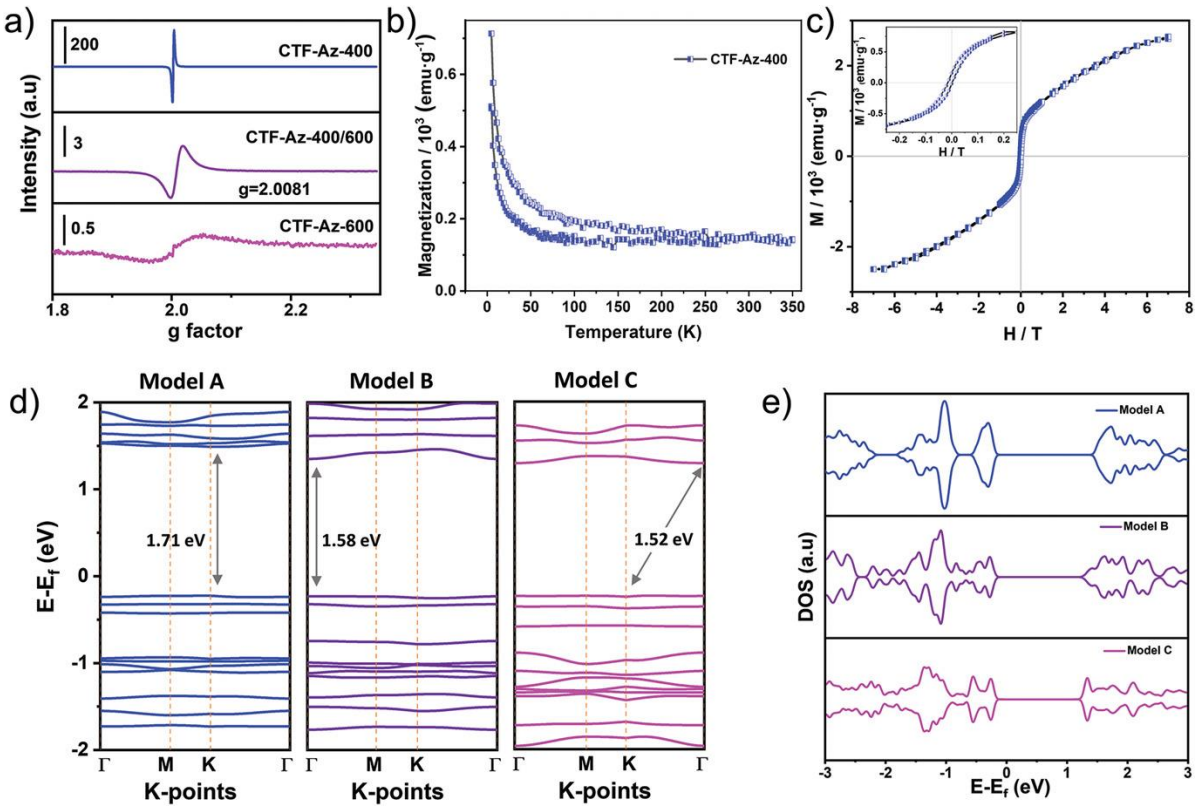

Figure 3 a) ESR spectra of CTF-Az-400/600, CTF-Az-400, and CTF-Az-600. b) Zero-field-cooled and field-cooled curves of CTF-Az-400 under an applied magnetic field of 100 Oe. c) Magnetic hysteresis loops obtained at 300 K. d) Band structures calculated with Γ (0, 0, 0), M (0.5, 0.5, 0), and K (0.33, 0.67, 0) and e) DOS spectra calculated using models A–C.

Benzenoid CTFs have been reported as promising electrode materials for numerous energy storage devices, including lithium-ion batteries,[29] sodium-ion batteries,[30] lithium–sulfur batteries,[31] and supercapacitors,[32] because of their high N content, rapid mass transport afforded by their rich porosity, and reversible ion insertion–deinsertion cycles afforded by their layered structure. In this study, we investigated the electrochemical potassium and lithium storage performance of CTF-Az-400/600 in half-cells by using K and Li foils as anodes in the voltage ranges of 1–4 V (versus K/K^+) and 1.5–4.5 V (versus Li/Li^+), respectively. The electrochemical properties were initially tested through cyclic voltammetry (CV; Figure S17a, Supporting Information) at a scan rate of 1 mV s^{-1} in the range of 1 and 4 V (versus K/K^+). The test results revealed a rectangular shape, suggesting a (de)potassiation behavior associated with the adsorption-desorption of K^+ ions.[33] Moreover, a galvanostatic charge–discharge test was conducted at current densities ranging from 0.2 to 10 A g^{-1}, and the results indicated that the charge-discharge curve (Figure S17b, Supporting Information) exhibited a sloping profile without an obvious voltage plateau, which is consistent with the trend of typical CV curves and suggests an adsorption-like feature.[33] Notably, the CTF-Az-400/600|K half-cell could endure 100 cycles with a stable reversible capacity of approximately 120 mA h g^{-1} at 1 A g^{-1} and Coulombic efficiency of >99% (Figure S17c, Supporting Information).[29, 30] The specific capacity values of the CTF-Az-400/600|K half-cell were 174, 133, 99, 94, and 90 mA h g^{-1} at 0.2, 0.5, 1, 2. 5, and 10 A g^{-1}, respectively (Figure S17d, Supporting Information).

The test results regarding the Li^+ storage performance of CTF-Az-400/600 also initially revealed a similar CV curve profile (Figure S18a, Supporting Information). Furthermore, we explored the rate capabilities of CTF-Az-400/600, as illustrated in Figure S18b, Supporting Information. The sample exhibited a specific capacity of 118.5 mAh g^{-1} at a low discharge rate

of 0.2 A g^{-1}. The specific capacity remained higher than 77.7 mAh g^{-1} at 20 A g^{-1}. When the discharge rate was reduced to 0.2 A g^{-1}, a capacity of 117.5 mAh g^{-1} was observed. Compared with the CTF-Az-400/600|K half-cell, the CTF-Az-400/600|Li half-cell showed higher cyclic stability, exhibiting a retained specific capacity of up to 112.2 mA h g^{-1} after 5000 cycles (Figure S18c, Supporting Information) as well as a Coulombic efficiency level of 99.5%; this finding indicates that the half-cell exhibited both chemically and thermally robust features.[34] The marginal increase in capacity with cycling suggests a gradual activation phenomenon caused by the infiltration of electrolytes into the porous matrix.[35] The superior Li^+ storage performance of the CTF-Az-400/600|Li half-cell was ascribed to the low charge-transfer resistance (R_{ct} = 46.71 Ω) of the half-cell (Figure S18f, Supporting Information), which was one-tenth of the value (457.8 Ω) derived for the CTF-Az-400/600|K half-cell (Figure S17f, Supporting Information). The mechanism underlying alkali-ion storage is described as follows: Sakaushi et al. reported that CTF-based cathodes work on the basis of continuous bipolar redox reactions, in which triazine exhibits both p- and n-doping features over a wide range of potentials during cycling.[30, 36] However, See et al. directly contradicted this viewpoint because they found that CTFs exhibit capacitive charge and discharge profiles and have substantial ESR signals that could contribute to the specific capacity, suggesting that the mechanism is not purely capacitive.[29] In this study, the CTF-Azs exhibited a similar capacitive characteristic. Additionally, in the presence of azulene, the CTF-Azs presented quantitative ESR signals, implying the existence of numerous unpaired spins, which could be beneficial for charge and discharge performance.[29] Notably, although the pore structure of CTF-Az-400/600 was reshaped at the cost of a few micropores, its total volume increased, which enhanced its electrochemical performance (Table 1).[37]

Typically, azulene rearrangement in naphthalene occurs at temperatures below 400 °C, but the azulene unit can exist in a framework structure owing to space-confining effects even at 1000 °C.[38] Hence, we prepared PCs with coexisting topological/heteroatom defects at controlled annealing temperatures of 800, 900, and 1000 °C without ammonia activation (denoted herein as PC-800, PC-900, and PC-1000, respectively) and with ammonia activation (denoted herein as PC-800a, PC-900a, and PC-1000a, respectively). We performed XPS to further investigate the chemical structures of these PCs. The XPS spectra of these PCs revealed typical N 1s peaks (Figure S19a, Supporting Information), with the derived N content being 0.42–1.45 at.% for the PCs prepared without ammonia activation, which was lower than that derived for the PCs prepared with ammonia activation (1.01–2.11 at.%); these results thus indicate that the N content can be well controlled through temperature and activation management. We also observed three C 1s deconvoluted peaks (Figure S19b, Supporting Information) at 284.5, 286.3, and 287.6 eV, which were attributed to the C-C/C=C, C=N, and C-N/C-O bonds, respectively, indicating the formation of graphitic fragments and covalently bonded N atoms.[13, 14] The resolved N 1s spectra (Figure S19c, Supporting Information) presented three peaks at 398.3, 401.1, and 403.1 eV, revealing the presence of pyridinic-N, graphitic-N, and pyridinic-N^+□O^- groups, respectively.

The XRD patterns (Figure S20b, Supporting Information) of the PCs presented two broad peaks at approximately 26° and 43°, which corresponded to the (002) and (100) lattice planes of graphite, respectively, suggesting the amorphous nature of the PCs. Moreover, the Raman spectra (Figure S20c, Supporting Information) showed that the I_D/I_G ratios derived for the PCs prepared without ammonia activation ranged from 0.98 to 1.08, which were higher than that derived for CTF-Az-400/600 (0.91). The PCs demonstrated an increased number of defects, which was due to the removal of doped N atoms and azulene-type topological defects.[22, 39] Clearly, the number of disordered carbon structures increased with temperature.[40] The nitrogen sorption isotherms (Figures S21 and S22, Supporting Information) of the PCs prepared without

and with ammonia activation were determined to be type-IV isotherms, and the corresponding pore size distribution curves presented microporous and mesoporous structures. The Brunauer–Emmett–Teller SSAs of PC-800, PC-900, and PC-1000 were 1551, 1478, and 1526 $m^2\ g^{-1}$, respectively (Table 1), which are lower than that of CTF-Az-400/600 (1716 $m^2\ g^{-1}$). This decrease in SSA was ascribed to the collapse of pore tunnels in the polymer during pyrolysis.[41] We also observed that PC-900a exhibited a higher SSA (1847 $m^2\ g^{-1}$) than PC-800a (1607 $m^2\ g^{-1}$) and PC-1000a (1701 $m^2\ g^{-1}$). Furthermore, TEM images of the PCs (Figures S23 and S24, Supporting Information) demonstrated that these samples exhibited similar morphological patterns that were composed of irregular stripes corresponding to randomly orientated graphite layers and disordered structures, which were ascribed to amorphous and defective carbon structures. EDS elemental mapping also revealed homogeneously distributed C and N atoms in the PCs. These results were not consistent with our expectation because we predicted the SSAs of these PCs to be extremely small owing to the possible decomposition of azulene and the framework structure. Accordingly, the findings indicate that our proposed strategy offers a new and rational approach for synthesizing CTF-Az-derived PCs with rich porosity and ultrahigh SSAs.

We applied XPS to detect all types of N components in the PCs, indicating the conversion process became complex because the total content of N decreases significantly as the temperature increases (**Figure** 4a).[30, 42] During pyrolysis, decomposition and recombination could inevitably lead to defects, such as pores and edges. Accordingly, we proposed that a sample could be converted into a PC structure while retaining five-seven-membered rings (Figure 4b); we examined this proposal through an ORR simulation. A highly interconnected framework with an ultrahigh SSA is generally believed to facilitate the effective exposure of active sites and the transportation of electrons and ions.[43] To explore the electrocatalytic activity of the PCs, we examined their ORR performance under an alkaline condition (0.1 M KOH). The resulting potentials were calibrated to a reversible hydrogen electrode. CV tests were first performed on O_2^- and N_2^- saturated solutions on a rotating disk electrode at a scan rate of 100 mV s^{-1} and a catalyst loading of 0.364 mg cm^{-2}. As displayed in Figure S25, Supporting Information, distinct ORR peaks were observed for the O_2^- saturated electrolyte, demonstrating the catalytic activity of CTF-Az-400/600 and the PCs. The ORR peak potentials of PC-900, PC-1000, PC-900a, and PC-1000a were approximately 0.682 V, which was higher than those of PC-800 (0.657 V), PC-800a (0.667 V), and CTF-Az-400/600 (0.628 V); this thus indicates that PC-800, PC-800a, and the CTF-Azs were more suitable for ORR. Linear sweep voltammetry (LSV) was also performed at a constant rotation rate of 1600 rpm, and the LSV curves are illustrated in Figure 4c and Figures S26–28, Supporting Information. The configured onset potential (E_o), half-wave potential ($E_{1/2}$), and limited current density (j_L) values are summarized in Table S2, Supporting Information. PC-1000 achieved a significant positive E_o (0.861 V) and the largest j_L (5.37 mA cm^{-2}), which were comparable to those of PC-900 (0.856 V versus 5.2 mA cm^{-2}) but superior to those of PC-800 (0.822 V versus 4.69 mA cm^{-2}). Compared with the PCs prepared without ammonia activation, those prepared with ammonia activation presented more positive E_o and larger j_L values, which could be ascribed to an increased proportion of pyridinic-N species and SSAs after ammonia activation. PC-900a had the most positive E_o (0.866 V) and $E_{1/2}$ (0.781 V), which were determined to be comparable to those of Pt/C (E_o = 0.895 V, $E_{1/2}$ = 0.814 V). Notably, the j_L value of PC-900a was up to 5.7 mA cm^{-2}, which was determined to be considerably higher than that of Pt/C (5.5 mA cm^{-2}). According to the LSV curves, the Tafel slopes observed in the polarized linear regions (Tafel region, Figure S27b, Supporting Information) for CTF-Az-400/600 (53 m $Vdec^{-1}$) and the PCs (65 m $Vdec^{-1}$ for PC-800, 77 m $Vdec^{-1}$ for PC-900, and 75 m $Vdec^{-1}$ for PC-1000) were less steep than that observed for Pt/C (97 m $Vdec^{-1}$), indicating a more favorable ORR kinetic

process in CTF-Az-400/600. Moreover, the Tafel slopes observed for PC-Ta ranged from 76 to 95 mV per decade, which were comparable to those observed for Pt/C (Figure 4d).

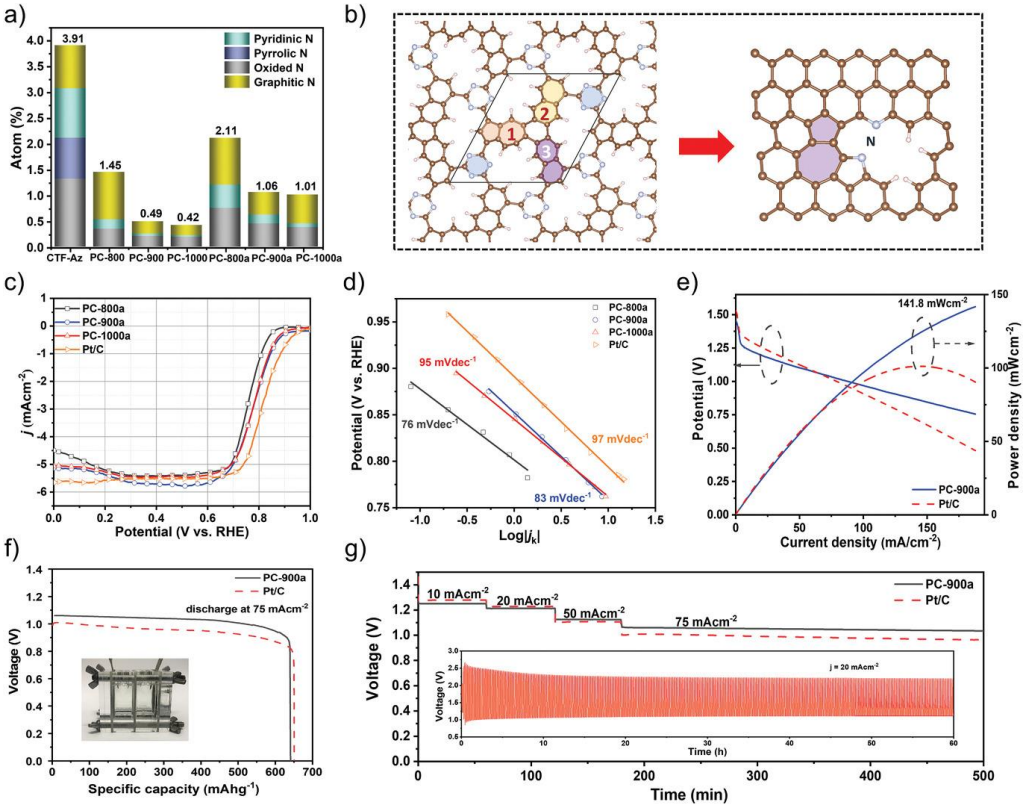

Figure 4 a) Atomic percentages of oxidized-N, graphitic-N, and pyridinic-N in the CTF-Az-400/600, PC-T, and PC-Ta (T = 800, 900, and 1000 °C) samples. b) Schematic of the conversion of CTFs into carbon materials. The ORR performance of PC-Ta samples and the performance of the Zn–air battery with PC-900a as a catalyst are also evaluated. c) LSV curves of PC-Ta. d) Tafel plots of PC-Ta. e) Discharge polarization curves and corresponding power density plots. f) Curves of galvanostatic discharge at 75 mA cm^{-2} until complete consumption of the Zn foil anode. Inset: Image of laboratory-assembled Zn–air battery. g) Long-term galvanostatic discharge curve at different current densities. Inset: Charge-discharge cycling performance of rechargeable Zn–air battery at 20 mA cm^{-2}.

To further understand the ORR kinetics, Koutechý-Levich (*K-L*) plots (Figures S26 and S28, Supporting Information) were obtained through LSV at rotation rates of 225–2025 rpm. We noted a good linear relationship between j^{-1} and $\omega^{-1/2}$ at voltages ranging from 0.2 to 0.6 V. In addition, the number of transferred electrons (n), as determined using the *K–L* equation, was approximately 4.0, suggesting a direct four-electron pathway.[44] For confirmation, we used a rotating ring-disk electrode (RRDE) for analysis, which also demonstrated a similar n (≈4; Figures S29 and S30, Supporting Information). The peroxide species (HO_2^-) formed during the ORR process were quantified using RRDE analysis. The HO_2^- yields detected at potentials ranging from 0.2 to 0.6 V were lower than 20%, corroborating that O_2 molecules were directly reduced to OH^- with high selectivity.[18, 45] Electrochemical impedance spectroscopy (EIS)was conducted to assess the ORR kinetics, and the results are displayed in Figure S31, Supporting Information; the semicircles in the high-frequency region were attributed to interface charge-transfer resistance.[19, 39] As indicated in this figure, the semicircles for PC-800 and PC-800a were larger than those for the other samples, suggesting a slower charge transfer, which degraded the ORR performance of the PC. By contrast, the semicircle for PC-900a was smaller in the high-frequency region, indicating a faster charge transfer. Furthermore, PC-900a had

good durability, as revealed by its current-time chronoamperometric response curve (Figure S32a, Supporting Information). The ORR current retention of this PC was as high as 81% after 40 000 s of operation. Remarkably, compared with Pt/C, PC-900a exhibited superior methanol tolerance with slight current degradation (<5%; Figure S32b, Supporting Information).

We also conducted an oxygen evolution reaction (OER) activity assessment under the same alkaline condition. According to the LSV curves (Figure S33a and Table S3, Supporting Information), PC-900a presented the best OER performance, with the sample exhibiting the highest negative overpotential (1.754 V) at 10 mA cm^{-2} ($E_{j = 10}$). Notably, PC-900a exhibited a smaller potential gap (ΔE = 973 mV) between $E_{j = 10}$ (OER) and $E_{1/2}$ (ORR), demonstrating its superior bifunctional catalytic activity (Figure S33c and Table S3, Supporting Information). The excellent electrocatalytic activity of the PCs can be ascribed to the synergistic effect of SSAs, N content, pyridinic content, and charge-transfer impedance.[46] Specifically, PC-900a possessed the highest SSA, highest N content, highest pyridinic-N content, and lowest charge-transfer resistance among all PCs, which eventually contributed to its state-of-the-art performance.

A comprehensive comparative analysis revealed that among all PCs prepared with ammonia activation, PC-900a exhibited the highest performance in terms of ORR activity and kinetics. In addition, we performed a proof-of-concept study by constructing a rechargeable Zn–air battery (Figure 4f, inset) to evaluate the utility of the bifunctional catalyst PC-900a. PC-900a was uniformly loaded onto a carbon fiber paper at a loading mass of 1 mg cm^{-2} as the cathode, and a Zn foil was used as the anode. The electrolyte was composed of 6 M KOH and 0.1 M $ZnCl_2$. We then plotted a discharge polarization curve and the corresponding power density curve (Figure 4e), which revealed that PC-900a had a high open voltage (1.45 V) and that its highest power density was 141.8 mW cm^{-2}, considerably higher than that of Pt/C (101.1 mW cm^{-2}). Moreover, the PC-900a-based Zn-air battery showed no obvious decline in power density at higher discharge voltages and higher current densities (>65 mA cm^{-2}), suggesting the preferable performance of PC-900a at high current densities. When discharged at 75 mA cm^{-2} (Figure 4f), the PC-900a-based battery exhibited a specific capacity of 650 mA h g^{-1}, which was determined to be comparable to that of Pt/C (650 mA h g^{-1}). The corresponding energy density was derived to be 666.4 W h kg^{-1}, which was noted to be higher than that of Pt/C by 49.2 W h kg^{-1}. Furthermore, galvanostatic discharge measurements were performed at current densities ranging from 10 to 75 mA cm^{-2} (Figure 4g). The results indicated that all discharge voltages were flat at all current densities, indicating favorable stability (Figure 4g, inset). Notably, at a high current density (75 mA cm^{-2}), the discharge potential of the PC-900a-based battery was higher than that of Pt/C by 0.07 V. As illustrated in the inset of Figure 4g, the battery had a small charge/discharge voltage gap (1.08 V) along with a stable and high discharge voltage (1.12 V) after being discharged at 20 mA cm^{-2} for 60 h.

To obtain insight into the possible mechanism underlying the ORR process for the PCs, we applied DFT to calculate the free energy in the reaction pathway. A typical model for nitrogen-doped carbon was constructed, as illustrated in **Figure** 5a; in this model, several defects were considered, including non-hexagonal ring defects and pyridinic-N defects. Several N and C configurations were considered as active sites for ORR catalysis.[47] On the basis of the associative mechanism, in which the energy barrier for carbon materials is usually relatively low, we considered five steps in the calculations:[48] 1) adsorption of O_2 molecules onto the catalyst surface; 2) reduction of $*O_2$ molecules to *OOH through H_2O and one-electron transfer; 3) cleavage of the O-O bond in *OOH to form an *O atom driven by a second-electron transfer; 4) reduction of the *O atom through H_2O and one-electron transfer to form an adsorbed *OH intermediate; and 5) dissolution from *OH to OH^- through direct one-electron reduction

(*O_2, *O, *OH, and *OOH represent adsorbed intermediates). A comparison of the Δ*G* values between two consecutive steps revealed that ΔG4 from *O to *OH must overlap the highest energy barrier of N atoms and the C5 site (Figure 5b). For C1—an active site—step 2 (O_2 → *OOH) was a rate-limiting step; moreover, O_2 adsorption dominated the entire reaction pathway at C4, C7, and all carbon atom sites that were not directly adjacent to the N atoms (Figure 5c,d). According to these free energy profiles (Figure 5b–d, Figures S34–43 and Table S6, Supporting Information), we observed that the lowest overpotential was 0.58 V, which was detected during O_2 adsorption at C6; this adsorption was an endothermic process that decelerated the entire turnover process.[49] A similar trend was observed at C8, which was associated with the highest energy barrier (0.63 eV; Figure 5d). This suggests that theoretically, carbon atoms that were not directly adjacent to the N atoms were more favorable for the ORR process. The various charge densities revealed the charge effects that tuned the electronic configuration of the neighboring carbon atoms (Figure 5e).[50] We found apparent charge accumulation (yellow region) on the part of five-seven membered ring and N doped five-ring after *O intermediate bonded with the edge carbon. This result firmly suggests an electron rearrangement.

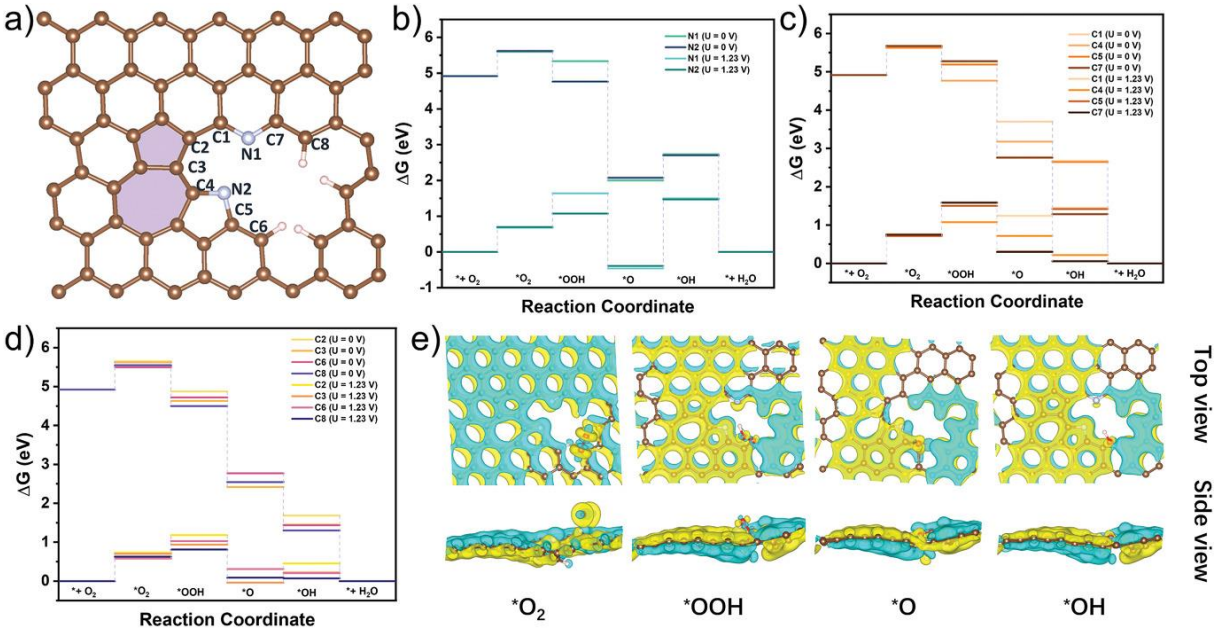

Figure 5 Theoretical simulations of an ORR involving PCs. a) Schematic of a PC structure containing an azulene unit doped with both pyridinic-N and pyrrole-N; active C and N sites are signed separately in order. Free energy diagrams of the ORR on b) N atoms, c) carbon atoms next to N atoms, and d) carbon atoms not directly adjacent to N atoms at U = 0 V and U = 1.23 V. e) Differential charge density distribution of PCs in the ORR at C6.

3 Conclusion

In summary, we prepared and studied CTF-Azs to explore the transition from porous polymers to PCs. According to DFT and structural analysis results, CTF-Azs prepared at low temperatures (e.g., 400 °C) were polymer frameworks, whereas those prepared at temperatures exceeding 400 °C exhibited the features of partially PCs. We noted that PCs with both topological and heteroatom defects could be practically prepared through the direct pyrolysis and activation of CTFs at high temperatures. Because of the azulene-type topological defects, nitrogen doping, high SSAs, and small charge-transfer impedance, the prepared PCs could function as electrocatalysts in ORR processes and in Zn-air batteries; for these PCs, the highest power density and specific capacity were 141.8 mW cm^{-2} and 650 mA h g^{-1}, respectively. DFT

calculations indicated that the N-doped carbon model with five-seven-membered rings synergistically contributed to the catalytic performance.

Acknowledgements

K.J .and P.P. contributed equally to this work. This work was financially supported by the NSFC (52173205, 51973114, 21720102002), and the Science and Technology Commission of Shanghai Municipality (19JC412600). The authors thank the support from Instrumental Analysis Center, Center for High Performance Computing at Shanghai Jiao Tong University. The authors thank the Catalysis and Surface Science Endstation at the BL11U beamline in the National Synchrotron Radiation Laboratory (NSRL) for help in the characterizations.

Conflict of Interest

The authors declare no conflict of interest.

Reference

1a) P. Kuhn, M. Antonietti, A. Thomas, Angew. Chem., Int. Ed. 2008, 47, 3450;

b) Y. Xu, S. Jin, H. Xu, A. Nagai, D. Jiang, Chem. Soc. Rev. 2013, 42, 8012;

c) C. S. Diercks, O. M. Yaghi, Science 2017, 355, eaal1585;

d) M. Mahato, R. Tabassian, V. H. Nguyen, S. Oh, S. Nam, W.-J. Hwang, I.-K. Oh, Nat. Commun. 2020, 11, 5358.

2a) S. Ren, M. J. Bojdys, R. Dawson, A. Laybourn, Y. Z. Khimyak, D. J. Adams, A. I. Cooper, Adv. Mater. 2012, 24, 2357;

b) S.-Y. Yu, J. Mahmood, H.-J. Noh, J.-M. Seo, S.-M. Jung, S.-H. Shin, Y.-K. Im, I.-Y. Jeon, J. -. B. Baek, Angew. Chem., Int. Ed. 2018, 57, 8438;

c) M. Mahato, S. Nam, R. Tabassian, S. Oh, V. H. Nguyen, I.-K. Oh, Adv. Funct. Mater. 2022, 32, 2107442;

d) R. Sun, X. Wang, X. Wang, B. Tan, Angew. Chem., Int. Ed. 2022, 61, e202117668.

3R. Kulkarni, Y. Noda, D. Kumar Barange, Y. S. Kochergin, P. Lyu, B. Balcarova, P. Nachtigall, M. J. Bojdys, Nat. Commun. 2019, 10, 3228.

4a) X. Hu, Z. Zhan, J. Zhang, I. Hussain, B. Tan, Nat. Commun. 2021, 12, 6596;

b) M. Liu, C. Wei, H. Zhuzhang, J. Zhou, Z. Pan, W. Lin, Z. Yu, G. Zhang, X. Wang, Angew. Chem., Int. Ed. 2022, 61, e202113389;

c) X. Suo, F. Zhang, Z. Yang, H. Chen, T. Wang, Z. Wang, T. Kobayashi, C.-L. Do-Thanh, D. Maltsev, Z. Liu, S. Dai, Angew. Chem., Int. Ed. 2021, 60, 25688;

d) T. Sun, Y. Liang, Y. Xu, Angew. Chem., Int. Ed. 2022, 61, e202113926;

e) C. He, Q.-J. Wu, M.-J. Mao, Y.-H. Zou, B.-T. Liu, Y.-B. Huang, R. Cao, CCS Chem. 2021, 3, 2368;

f) D.-L. Meng, M.-D. Zhang, D.-H. Si, M.-J. Mao, Y. Hou, Y.-B. Huang, R. Cao, Angew. Chem., Int. Ed. 2021, 60, 25485.

g) J.-D. Yi, R. Xu, Q. Wu, T. Zhang, K.-T. Zang, J. Luo, Y.-L. Liang, Y.-B. Huang, R. Cao, ACS Energy Lett. 2018, 3, 883.

h) M. Zhang, J. Yi, Y. Huang, R. Cao, Chinese J. Struc. Chem 2021, 40, 1213.

5 C. E. Chan-Thaw, A. Villa, P. Katekomol, D. Su, A. Thomas, L. Prati, Nano Lett. 2010, 10, 537.

6a) X. Zhu, C. Tian, S. M. Mahurin, S.-H. Chai, C. Wang, S. Brown, G. M. Veith, H. Luo, H. Liu, S. Dai, J. Am. Chem. Soc. 2012, 134, 10478;

b) A. Bhunia, D. Esquivel, S. Dey, R. Fernández-Terán, Y. Goto, S. Inagaki, P. Van Der Voort, C. Janiak, J. Mater. Chem. A 2016, 4, 13450;

c) W. Huang, N. Huber, S. Jiang, K. Landfester, K. A. I. Zhang, Angew. Chem., Int. Ed. 2020, 59, 18368.

7 E. Troschke, S. Grätz, T. Lübken, L. Borchardt, Angew. Chem., Int. Ed. 2017, 56, 6859.

8a) Z.-A. Lan, Y. Fang, X. Chen, X. Wang, Chem. Commun. 2019, 55, 7756;

b) W. Huang, Q. He, Y. Hu, Y. Li, Angew. Chem., Int. Ed. 2019, 58, 8676.

9 A. García-Sánchez, M. Gomez-Mendoza, M. Barawi, I. J. Villar-Garcia, M. Liras, F. Gándara, V. A. De La Peña, O'Shea, J. Am. Chem. Soc. 2020, 142, 318.

10a) K. W. Nam, S. S. Park, R. Dos Reis, V. P. Dravid, H. Kim, C. A. Mirkin, J. F. Stoddart, Nat. Commun. 2019, 10, 4948;

b) J. Wang, C. S. Chen, Y. Zhang, ACS Sustainable Chem. Eng. 2018, 6, 1772;

c) O. Buyukcakir, J. Ryu, S. H. Joo, J. Kang, R. Yuksel, J. Lee, Y. Jiang, S. Choi, S. H. Lee, S. K. Kwak, S. Park, R. S. Ruoff, Adv. Funct. Mater. 2020, 30, 2003761;

d) Y. Zheng, S. Xia, F. Dong, H. Sun, Y. Pang, J. Yang, Y. Huang, S. Zheng, Adv. Funct. Mater. 2021, 31, 2006159.

11 M. Liu, L. Guo, S. Jin, B. Tan, J. Mater. Chem. A 2019, 7, 5153.

12 Y. Zhao, K. X. Yao, B. Teng, T. Zhang, Y. Han, Energy Environ. Sci. 2013, 6, 3684.

13a) K. Schwinghammer, S. Hug, M. B. Mesch, J. Senker, B. V. Lotsch, Energy Environ. Sci. 2015, 8, 3345;

b) Y. Xiong, Y. Qin, L. Su, F. Ye, Chemistry 2017, 23, 11037.

14a) M. R. Liebl, J. Senker, Chem. Mater. 2013, 25, 970;

b) M. Liu, Q. Huang, S. Wang, Z. Li, B. Li, S. Jin, B. Tan, Angew. Chem., Int. Ed. 2018, 57, 11968.

15 W. Wang, H. Zhang, S. Zhang, Y. Liu, G. Wang, C. Sun, H. Zhao, Angew. Chem., Int. Ed. 2019, 58, 16644.

16 C. Lu, J. Yang, S. Wei, S. Bi, Y. Xia, M. Chen, Y. Hou, M. Qiu, C. Yuan, Y. Su, F. Zhang, H. Liang, X. Zhuang, Adv. Funct. Mater. 2019, 29, 1806884.

17 W. Che, W. Cheng, T. Yao, F. Tang, W. Liu, H. Su, Y. Huang, Q. Liu, J. Liu, F. Hu, Z. Pan, Z. Sun, S. Wei, J. Am. Chem. Soc. 2017, 139, 3021.

18 M. Zeng, Y. Liu, F. Zhao, K. Nie, N. Han, X. Wang, W. Huang, X. Song, J. Zhong, Y. Li, Adv. Funct. Mater. 2016, 26, 4397.

19 P. Chen, T. Zhou, L. Xing, K. Xu, Y. Tong, H. Xie, L. Zhang, W. Yan, W. Chu, C. Wu, Y. Xie, Angew. Chem., Int. Ed. 2017, 56, 610.

20a) C. Lu, D. Tranca, J. Zhang, F. Rodríguez Hernández, Y. Su, X. Zhuang, F. Zhang, G. Seifert, X. Feng, ACS Nano 2017, 11, 3933;

b) H. Yu, L. Shang, T. Bian, R. Shi, G. I. N. Waterhouse, Y. Zhao, C. Zhou, L.-Z. Wu, C.-H. Tung, T. Zhang, Adv. Mater. 2016, 28, 5080.

21a) K. Wu, L. Zhang, Y. Yuan, L. Zhong, Z. Chen, X. Chi, H. Lu, Z. Chen, R. Zou, T. Li, C. Jiang, Y. Chen, X. Peng, J. Lu, Adv. Mater. 2020, 32, 2002292;

b) L. Zhao, Y. Zhang, L.-B. Huang, X.-Z. Liu, Q.-H. Zhang, C. He, Z.-Y. Wu, L.-J. Zhang, J. Wu, W. Yang, L. Gu, J.-S. Hu, L.-J. Wan, Nat. Commun. 2019, 10, 1278.

22a) H.-Y. Jeong, M. Balamurugan, V. S. K. Choutipalli, E.-S. Jeong, V. Subramanian, U. Sim, K. T. Nam, J. Mater. Chem. A 2019, 7, 10651;

b) H. Zhao, C. Sun, Z. Jin, D.-W. Wang, X. Yan, Z. Chen, G. Zhu, X. Yao, J. Mater. Chem. A 2015, 3, 11736.

23 P. Pachfule, D. Shinde, M. Majumder, Q. Xu, Nat. Chem. 2016, 8, 718.

24 T.-T. Liu, R. Xu, J.-D. Yi, J. Liang, X.-S. Wang, P.-C. Shi, Y.-B. Huang, R. Cao, ChemCatChem 2018, 10, 2036.

25 C. Yang, K. S. Schellhammer, F. Ortmann, S. Sun, R. Dong, M. Karakus, Z. Mics, M. Löffler, F. Zhang, X. Zhuang, E. Cánovas, G. Cuniberti, M. Bonn, X. Feng, Angew. Chem., Int. Ed. 2017, 56, 3920.

26 Q. Jiang, T. Tao, H. Phan, Y. Han, T. Y. Gopalakrishna, T. S. Herng, G. Li, L. Yuan, J. Ding, C. Chi, Angew. Chem., Int. Ed. 2018, 57, 16737.

27a) J. Liu, S. Mishra, C. A. Pignedoli, D. Passerone, J. I. Urgel, A. Fabrizio, T. G. Lohr, J. Ma, H. Komber, M. Baumgarten, C. Corminboeuf, R. Berger, P. Ruffieux, K. Müllen, R. Fasel, X. Feng, J. Am. Chem. Soc. 2019, 141, 12011;

b) S. Thomas, S. Ramasesha, K. Hallberg, D. Garcia, Phys. Rev. B 2012, 86, 180403.

28 C. Yang, R. Dong, M. Wang, P. S. Petkov, Z. Zhang, M. Wang, P. Han, M. Ballabio, S. A. Bräuninger, Z. Liao, J. Zhang, F. Schwotzer, E. Zschech, H.-H. Klauss, E. Cánovas, S. Kaskel, M. Bonn, S. Zhou, T. Heine, X. Feng, Nat. Commun. 2019, 10, 3260.

29a) K. A. See, S. Hug, K. Schwinghammer, M. A. Lumley, Y. Zheng, J. M. Nolt, G. D. Stucky, F. Wudl, B. V. Lotsch, R. Seshadri, Chem. Mater. 2015, 27, 3821;

b) B. Wang, A. J. Fielding, R. A. W. Dryfe, Chem. Commun. 2018, 54, 3827;

c) B. Wang, V. Likodimos, A. J. Fielding, R. A. W. Dryfe, Carbon 2020, 160, 236.

30a) J. Zhu, X. Zhuang, J. Yang, X. Feng, S.-I. Hirano, S.-I. Hirano, J. Mater. Chem. A 2017, 5, 16732;

b) K. Sakaushi, E. Hosono, G. Nickerl, T. Gemming, H. Zhou, S. Kaskel, J. Eckert, Nat. Commun. 2013, 4, 1485.

31a) E. Jin, M. Asada, Q. Xu, S. Dalapati, M. A. Addicoat, M. A. Brady, H. Xu, T. Nakamura, T. Heine, Q. Chen, D. Jiang, Science 2017, 357, 673;

b) S. N. Talapaneni, T. H. Hwang, S. H. Je, O. Buyukcakir, J. W. Choi, A. Coskun, Angew. Chem., Int. Ed. 2016, 55, 3106.

32a) Y. Li, S. Zheng, X. Liu, P. Li, L. Sun, R. Yang, S. Wang, Z. -. S. Wu, X. Bao, W. -. Q. Deng, Angew. Chem., Int. Ed. 2018, 57, 7992;

b) L. Hao, J. Ning, B. Luo, B. Wang, Y. Zhang, Z. Tang, J. Yang, A. Thomas, L. Zhi, J. Am. Chem. Soc. 2015, 137, 219.

33 W. Zhang, M. Sun, J. Yin, K. Lu, U. Schwingenschlögl, X. Qiu, H. N. Alshareef, Adv. Energy Mater. 2021, 11, 2101928.

34 X. Yang, Y. Hu, N. Dunlap, X. Wang, S. Huang, Z. Su, S. Sharma, Y. Jin, F. Huang, X. Wang, S.-H. Lee, W. Zhang, Angew. Chem., Int. Ed. 2020, 59, 20385.

35 H. Zhang, W. Sun, X. Chen, Y. Wang, ACS Nano 2019, 13, 14252.

36 K. Sakaushi, G. Nickerl, F. M. Wisser, D. Nishio-Hamane, E. Hosono, H. Zhou, S. Kaskel, J. Eckert, Angew. Chem., Int. Ed. 2012, 51, 7850.

37 R. Yuan, W. Kang, C. Zhang, Materials 2018, 11, 937.

38a) L. T. Scott, Acc. Chem. Res. 1982, 15, 52;

b) L. T. Scott, M. A. Kirms, J. Am. Chem. Soc. 1981, 103, 5875.

39a) C. Tang, B. Wang, H. -. F. Wang, Q. Zhang, Adv. Mater. 2017, 29, 1703185;

b) C. Tang, H.-F. Wang, X. Chen, B.-Q. Li, T.-Z. Hou, B. Zhang, Q. Zhang, M.-M. Titirici, F. Wei, Adv. Mater. 2016, 28, 6845;

c) Y. Jia, L. Zhang, A. Du, G. Gao, J. Chen, X. Yan, C. L. Brown, X. Yao, Adv. Mater. 2016, 28, 9532.

40 S. Mukherjee, M. Das, A. Manna, R. Krishna, S. Das, J. Mater. Chem. A 2019, 7, 1055.

41 J. P. Cheng, X. B. Zhang, Y. Ye, J. P. Tu, F. Liu, X. Y. Tao, H. J. Geise, G. V. Tendeloo, Microporous Mesoporous Mater. 2005, 81, 73.

42 Y. Su, Y. Liu, P. Liu, D. Wu, X. Zhuang, F. Zhang, X. Feng, Angew. Chem., Int. Ed. 2015, 54, 1812.

43 Q. Wang, Y. Ji, Y. Lei, Y. Wang, Y. Wang, Y. Li, S. Wang, ACS Energy Lett. 2018, 3, 1183.

44 X. Zhuang, F. Zhang, D. Wu, N. Forler, H. Liang, M. Wagner, D. Gehrig, M. R. Hansen, F. Laquai, X. Feng, Angew. Chem., Int. Ed. 2013, 52, 9668.

45 H. -W. Liang, Z.-Y. Wu, L.-F. Chen, C. Li, S.-H. Yu, Nano Energy 2015, 11, 366.

46a) K. N. Chaudhari, M. Y. Song, J.-S. Yu, Small 2014, 10, 2625;

b) P. Chen, T.-Y. Xiao, Y.-H. Qian, S.-S. Li, S.-H. Yu, Adv. Mater. 2013, 25, 3192;

c) S.-L. Cai, Y.-B. Zhang, A. B. Pun, B. He, J. Yang, F. M. Toma, I. D. Sharp, O. M. Yaghi, J. Fan, S.-R. Zheng, W.-G. Zhang, Y. Liu, Chem. Sci. 2014, 5, 4693.

47 D. Guo, R. Shibuya, C. Akiba, S. Saji, T. Kondo, J. Nakamura, Science 2016, 351, 361.

48 Y. Gao, Z. Cai, X. Wu, Z. Lv, P. Wu, C. Cai, ACS Catal. 2018, 8, 10364.

49 J. Liu, M. Jiao, L. Lu, H. M. Barkholtz, Y. Li, Y. Wang, L. Jiang, Z. Wu, D.-J. Liu, L. Zhuang, C. Ma, J. Zeng, B. Zhang, D. Su, P. Song, W. Xing, W. Xu, Y. Wang, Z. Jiang, G. Sun, Nat. Commun. 2017, 8, 15938.

50 N. Yang, L. Li, J. Li, W. Ding, Z. Wei, Chem. Sci. 2018, 9, 5795.